Reduction of environmentally induced cracking of laser-welded shape memory NiTi wires via post-weld heat-treatment

Chan, C. W., & Man, H. C. (2013). Reduction of environmentally induced cracking of laser-welded shape memory NiTi wires via post-weld heat-treatment. *Materials Science and Engineering: A*, *588*, 388-394. https://doi.org/10.1016/j.msea.2013.09.051

Published in:
Materials Science and Engineering: A

Document Version:
Peer reviewed version

Queen's University Belfast - Research Portal:
Link to publication record in Queen's University Belfast Research Portal

Reduction of Environmentally Induced Cracking of Laser-welded Shape Memory NiTi Wires via Post-weld Heat-treatment

C.W. Chan*[1], H.C. Man[2]

[1] School of Mechanical and Aerospace Engineering, Queen's University Belfast, Northern Ireland, UK

[2] Department of Industrial and Systems Engineering, The Hong Kong Polytechnic University, Hung Hom, Kowloon, Hong Kong, China

Abstract

In this study, the environmentally induced cracking behaviour of the NiTi weldment with and without post-weld heat-treatment (PWHT) in Hanks' solution at 37.5 °C at OCP were studied by tensile and cyclic slow-strain-rate tests (SSRT), and compared with those tested in oil (an inert environment). Our previous results in the tensile and cyclic SSRT showed that the weldment without PWHT showed high susceptibility to the hydrogen cracking, as evidenced by the degradation of tensile and super-elastic properties when testing in Hanks' solution. The weldment after PWHT was much less susceptible to hydrogen attack in Hanks' solution as no obvious degradation in the tensile and super-elastic properties was observed, and only a very small amount of micro-cracks were found in the fracture surface. The susceptibility to hydrogen cracking of the NiTi weldment could be alleviated by applying PWHT at the optimized temperature of 350 °C after laser welding.

Keywords: Post-weld Heat-treatment, Hydrogen Embrittlement, Shape Memory Alloys, Laser Welding, NiTi

*E-mail address of corresponding author: c.w.chan@qub.uk.ac

1. Introduction

Because of the shape memory and super-elastic effects (SME and SE) as well as good biocompatibility, NiTi has been used as biomaterials for various biomedical applications in the last decades [1-2]. NiTi is known to be susceptible to environmentally induced embrittlement in corrosive environments as detailed by Yokoyama et al. [3-6]. The environmentally induced brittle fracture is a consequence of the absorption of hydrogen generated in the electrochemical reactions of NiTi with an electrolyte [7].

Joining of NiTi is a difficult task because the SME and SE of NiTi are highly sensitive to the thermal stimuli in the joining process. With the ability to localize the heat input and to minimize the thermal induced defects, laser welding has been regarded as a suitable method for joining NiTi. The application of laser technology in welding NiTi has been well researched in the last decade, and basically the research direction can be grouped into two main categories. One is focused on the characterization of the mechanical and functional properties [8-15], while the other, on the evaluation of corrosion behaviours [16-18]. From the point of view of medical device applications, the NiTi weldment or components are simultaneously subjected to the corrosive body fluids under different types of cyclic and repetitive loadings, such as bending, tension, compression, or a mixed mode. However, the study on the mechanical and functional behaviours of the NiTi weldment in corrosive environments is still very limited.

It has been first reported by the present authors that the presence of thermal induced defects in the welded regions (weld zone, WZ and heat-affected zone, HAZ) promotes hydrogen

cracking in Hanks' solution at OCP subjected to mechanical loading [19]. This implies that certain post processing must be done after laser welding in order to make sure the NiTi weldment can function properly in the human body without any potential problems causing failure.

In this study, post-weld heat-treatment (PWHT) at proper temperature was applied to the weldment, and tried to reduce the susceptibility to hydrogen cracking in Hanks' solution at OCP. PWHT is usually recommended after laser-welding because it can reduce the thermal-induced defects and residual stress in the weldments [20, 21]. The positive effects of PWHT on the mechanical and functional as well as corrosion properties of the NiTi weldment have been reported in the authors' previous studies [20, 21].

2. Experimental Details

2.1 Materials and Procedure of Laser Welding

The materials used were annealed Ti-55.91 wt % Ni wire of 0.5 mm (purchased from Johnson Matthey). The sample surfaces were ground using 600 grit SiC papers before laser welding. Butt weld was made on two pieces of the NiTi wires using a 100-W CW fibre laser (Model SP-100C-0013, output wavelength 1091 nm). The beam was focused using a lens of focal length 91 mm and the spot size was 46 μm at the work piece. The welding process was performed under an argon shielding environment. The parameter settings to produce the weldments in this study were optimized by fractional factorial experimental design: 72 W in laser power, 115 ms in welding time, + 0 mm in defocusing, and 25 L/min in argon flow rate [22].

After laser welding, post-weld heat-treatment (PWHT) was applied on the weldments. The heat-treatment temperature was already optimized in the previous study, with 350 °C (or 623 K) showing the best in both the mechanical [21] and corrosion properties [23]. The PWHT was done by putting the weldment in the furnace at 350 °C for 3600 s, followed by water quenching. There were altogether three types of samples: as-received, as-welded, and heat-treated samples being tested and compared in the mechanical and corrosion tests in this study. The latter two were composed of the weld zone (WZ), heat-affected zone (HAZ) and base material (BM). All the samples were ground to 2400 grit surface finish and ultrasonically cleaned in distilled water, and acetone for 10 minutes before the mechanical and corrosion tests.

2.2 Characterization of Phase Structure and Transformation Temperatures

The samples were polished with 1-µm diamond paste and etched by a reagent (HF 10 %, HNO_3 40 %, H_2O 50 %) for cross-sectional metallographic characterization. The microstructural observations and fractographs were taken by scanning-electron microscopy (SEM, Model JSM-6490, JEOL, USA, Peabody, MA). The phase structure was identified by selected area diffraction (TEM, Model JEM-2010, JEOL, USA, Peabody, MA) and x-ray diffraction (XRD, Model D8 Discover X-ray diffractometer, Bruker Axs Inc., Madison, WI). A Perkin Elmer DSC 7 system (Waltham, MA) was used to study the phase transformation temperatures between the range of −70 °C and 100 °C at 10 °C/min.

2.3 Cyclic Polarization Tests in Hanks' solution

The corrosion resistance was evaluated by cyclic polarization tests in Hanks' solution at 37.5 °C. The compositions of Hanks' solution was as NaCl 8 g/l, Na_2HPO_4 0.0475 g/l, $NaHCO_3$ 0.35 g/l, KCl 0.4g/l, KH_2PO_4 0.06 g/l, $MgCl_2$-$6H_2O$ 0.10 g/l, $MgSO_4$-$7H_2O$ 0.10 g/l, $CaCl_2$ 0.18 g/l, and glucose 1 g/l. The cyclic polarization tests were performed conforming to ASTM Standard G61-86 [24] by a potentiostat (EG&G Princeton Applied Research (PAR), model 273A), with the saturated calomel electrode (SCE) and graphite rods being used as the reference and counter electrodes respectively. The scan started from 250 mV_{SCE} below the OCP at a sweep rate of 0.5 mV s^{-1} after an initial delay of 3600 s. The scan was reversed when a current density of 5 mA cm^{-2} was reached, and continued until the hysteresis loop closed.

2.4 Tensile and Cyclic SSRT in Hanks' solution at OCP

Slow-strain-rate tests (SSRT) were carried out with a strain rate of 10^{-6} s^{-1} using an INSTRON tensile machine with a load cell of 2 kN (INSTRON is a trademark of Instron, Canton, MA). The samples were immersed in the corrosion cell filled with 250 mL of Hanks' solution kept at 37.5 °C at OCP. The Hanks' solution was continuously pumped from a container which was immersed in a temperature-controlled water bath. The samples were 0.5 mm in diameter and 150 mm in gauge length. The exposed area to the solution was controlled to be 0.5 cm^2. The samples were loaded from 0 MPa until fracture.

In addition to the strain-to-fracture tests (or tensile SSRT), cyclic SSRT was also carried out. The samples were subjected to 10 complete cycles of tensile loading to a maximum elongation of 4 % and subsequent unloading to a stress of 5 MPa. The stress-strain hystereses were automatically recorded. During the cyclic SSRT, the open-circuit potential (OCP) was simultaneously recorded by the PAR 273A potentiostat. The SCE was used as the reference electrode.

2.5 EIS Measurements in Hanks' solution after Cyclic SSRT

Electrochemical impedance spectroscopic (EIS) measurements were carried out by means of a frequency response detector coupled to the PAR 273A potentiostat. A sine wave of 10 mV in amplitude was applied to the samples after cyclic SSRT in Hanks' solution at 37.5 °C at open-circuit potential (OCP), and the impedance spectra of the samples were acquired in the frequency range from 100 kHz to 1 mHz.

3. Results

3.1 Phase Structure and Transformation Temperature Analyses

It has been shown in the authors' previous work [25, 26] that the NiTi weldment exhibited a dendritic structure in the WZ due to the rapid solidification effect and a coarse equiaxed grain structure in the HAZ due to the gradient effect of re-crystallization by heat conduction in the wire. For the heat-treated sample in this study, the SEM micrographs (Fig. 1a-c) indicated that it still showed a dendritic structure in the WZ and a re-crystallized equiaxed grain structure in the HAZ, with a little increase in grain size. The XRD patterns for different samples are given in Fig. 2. The as-welded sample showed a close similarity to the microstructure as observed in the as-received sample, being composed of the primary B2 phases in the matrix without any precipitates. Apart from the primary B2 phases, a small amount of the B19' phases and Ni_4Ti_3 precipitates were observed in the heat-treated sample. The existence of Ni_4Ti_3 particles in the heat-treated sample was further confirmed by TEM analysis. The fine and coherent Ni_4Ti_3 precipitates (about 10 nm in size) nucleated and grew in the plane parallel to the parent B2 phases as observed in the TEM micrograph and supported by the selected area diffraction patterns (SADP) in Fig. 3.

The Ni_4Ti_3 precipitates have rhombohedral structure and are usually formed at annealing temperatures below 680 K as fine platelets with coherency to the matrix [27]. The precipitation of Ni_4Ti_3 particles causes local Ni depletion (or equivalently enrichment of Ti) in the NiTi matrix, and shifts the phase transformation to higher temperatures [28]. The transformation temperatures

of different samples are given in Table 1.

From the DSC results, the austenite and martensite coexist in the matrix when the heat-treated weldment is at room temperature (or 25 °C), because of the incomplete martensite-to-austenite transformation. As a result, some B19’ phases were found in the XRD patterns of the heat-treated sample. In the tensile and cyclic SSRT, the testing temperature was held constantly at 37.5 °C to mimic the human body temperature and to guarantee the samples were in the austenite phase that exhibits fully super-elastic property.

3.2 Cyclic Polarization Tests in Hanks' solution

The corrosion resistance of NiTi originates from the formation of passive titanium oxide layer when immersing in an aqueous solution. The passive layer is usually of a few hundreds nanometers in thickness, and its resistance to corrosion is evaluated by cyclic polarization test and electrochemical impedance spectroscopy (EIS). The polarization curves for various samples in Hanks' solution are depicted in Fig. 4, and values of the corrosion potential (Ecorr), pitting potential (Epit) and corrosion current density (Icorr) extracted from the curves are given in Table 2. It can be observed from the polarization curves that corrosion resistance of the heat-treatment sample was comparable to the as-received sample, and meanwhile was higher than that of the as-welded sample as evidenced by the higher values of Ecorr, Epit and Icorr.

3.3 Tensile and Cyclic SSRT in Hanks’ solution at OCP

The stress-strain curves for various samples obtained in oil and in Hanks’ solution are given in Fig. 5 and Fig. 6 respectively. As observed in the figures, the tensile strength and breakdown

strain of the samples tested in Hanks' solution were found to decrease as compared to those tested in oil. The decrease in the tensile strength and breakdown strain for the as-received and heat-treatment sample was very small, while the as-welded sample showed more reduction in the tensile properties. Moreover, the stress plateau, which represents the onset and end of stress-induced martensitic transformation (SIMT) process, of the samples tested in Hanks' solution was fluctuating and gradually growing upward, while the samples tested in oil remained stable and flat. This indicated the SIMT process was affected by Hanks' solution, and more stress was required to induce the transformation process. It is particular to note that the stress plateau of the heat-treated sample was lower than other samples. The fractographs for the as-welded and heat-treated samples after tensile SSRT in Hanks' solution are given in Fig. 7a-b and Fig. 7c-d respectively. It is quite clear that more micro-cracks and welding defects were present in the fracture surface of the as-welded sample, when compared to the sample after being heat-treated.

On the other hand, an important measure for the super-elasticity of NiTi is the amount of residual strain left after loading and unloading. The smaller the residual strain, the better the super-elasticity. The accumulated residual strain curves (up to 10 cycles) for various samples after cyclic SSRT in oil and Hanks' solution are given in Fig. 8. As observed in the figure, the accumulated residual strain of the samples tested in Hanks' solution was larger than those in oil. For the results in Hanks' solution, the as-received sample showed that smallest amount of accumulated residual strain after cycling loading, followed by the heat-treated sample, with the as-welded sample being the highest. This indicated that the accumulated residual strain of the

sample after being heat-treated was partially recovered.

The OCP curve of the heat-treated sample recorded throughout cyclic SSRT in Hanks' solution is shown in Fig. 9, and then compared with the as-welded and as-received samples as given in Fig. 10. It can be observed from Fig. 10 that the OCP signal responded dynamically with the cyclic stress-strain curve. Comparing with the unloading cycle, the OCP in the loading cycle was in general smaller and reached its minimum at the onset of the stress-induced martensitic transformation (SIMT). This phenomenon has been reported in details in the authors' previous study [19].

When looking at Fig. 10, the OCP pattern of the heat-treated sample was more stable and the value kept rising in a quite constant rate throughout the test, whilst the as-welded sample was more unstable and widely scattered in the first cycle, yet a rising trend can still be observed. The higher value of the OCP throughout the test also indicated that the heat-treated sample was more corrosion-resistant than the as-welded sample.

3.4 EIS Measurements in Hanks' solution after Cyclic SSRT at OCP

The EIS data acquired at OCP in Hanks' solution after cyclic SSRT are shown in the Nyquist plots and Bode plots in Fig. 11a and 11b respectively. The data indicated that all the Nyquist plots only exhibited one time constant in the frequency range studied, and therefore the sample-electrolyte interface can be modeled by a simple equivalent circuit (EC) that consists of an active electrolyte resistance (R_S) in series with the parallel combination of a capacitance (C) and a polarization (or corrosion) resistance (Rp). The Rp is deduced from the curve fitting of

semicircular Nyquist plots by the software: Zview. When comparing the Rp between the two weldments after cyclic SSRT, the Rp of the heat-treated sample was at least two times higher than the as-welded sample. Comparing to the as-received sample, the Rp of the heat-treated sample was slightly smaller. The results in the EIS test were agreed well with those obtained in the cyclic polarization test, suggesting the ranking of corrosion resistance in the descending order of as-received > heat-treated > as-welded samples.

4. Discussions

When straining NiTi in the super-elastic regime in saline solution, atomic hydrogen as a consequence of repassivation would be absorbed by NiTi and located at the microstructural defects, such as dislocations and twin boundaries [29, 30]. The absorbed hydrogen atoms could interfere with the stress-induced martensitic transformation (SIMT) by (i) raising the critical stress level required for martensitic transformation and (ii) increasing the amount of accumulated residual strain after cyclic loading on account of more stress-induced martensite cannot transform back to austenite and become residual in the parent phase [19].

Because of the severe local plastic deformation and welding defects in the welded regions (WZ and HAZ) where acting as hydrogen trapping sites [19], the as-welded sample showed a high susceptibility to hydrogen cracking in Hanks' solution when subjected to tensile or cyclic loading, comparing to that tested in oil. The micro-cracks, which is believed to be the hydrogen-induced cracks, can be clearly found throughout the fracture surface (see Fig. 7a and 7b) after testing in Hanks' solution at OCP. It was firstly reported in this study that heat-treating

the weldment at 350 °C (or 673 K) can obviously reduce the susceptibility to hydrogen cracking in Hanks' solution at OCP, as evidenced by the smaller amount of accumulated residual strain after the cyclic SSRT and significantly reduced amount of micro-cracks in the fracture surface (see Fig 7c and 7d). Such improvement could be explained by (i) the reduced amount of dislocations acting as hydrogen trapping sites in the welded regions, and (ii) formation of more protective passive film onto the sample surfaces. Both of the effects are originating from the precipitation of coherent and fine Ni_4Ti_3 particles, i.e. about 10 nm in size, after post-weld heat-treatment.

In the first case, it has been widely reported that the fine and coherent Ni_4Ti_3 precipiates can resist the plastic flow by acting as effective barriers to dislocation motion [31-33]. As a result, the Ni_4Ti_3 precipitates in the heat-treated sample would increase the stress required for plastic flow in the welded regions and meanwhile suppress the formation of dislocations during straining, as evidenced by the smaller amount of residual strain after cyclic SSRT comparing to the as-welded sample.

It has been reported by Gall et al. [34, 35] that the precipitation of coherent Ni_4Ti_3 particles after heat treatment can greatly influence the critical stress level required for martensitic transformation by the generation of strong local stress fields between the precipitates and the NiTi matrix. Such local stress fields as a consequence of the lattice parameter mismatch between the precipitates and the matrix create preferential nucleation sites for martensitic transformation, and hence lower the critical stress level to induce the transformation process [36]. As a result, the

stress plateau of the heat-treated sample was lower than that of the as-welded sample.

However, it is worthwhile to note that size and coherency of the Ni_4Ti_3 precipitates are critical in affecting the mechanical and functional properties of the weldment [34-36]. Over-aging the weldment above 450 °C (or 723 K) has no benefit at all because the Ni_4Ti_3 precipitates would grow too large (more than a few hundreds of nanometers) and become incoherent with the matrix. It has been determined by Treppmann et al. [37] that the Ni_4Ti_3 precipitates are perfectly coherent with the matrix at about 10 nm and completely lose the coherency at about 300 nm.

In the second case, the precipitation of Ni_4Ti_3 particles would increase the overall Ti/Ni ratio in the heat-treated sample, and thereby enrich the passive film with higher amount of Ti. The enrichment of Ti content in the surface passive film would make the heat-treated sample more corrosion resistant in Hanks' solution [38], as evidenced by the higher values of Ecorr, Epit and Icorr in the cyclic polarization tests, OCP in the cyclic SSRT and Rp in the EIS measurements when comparing to the as-welded sample.

5. Conclusions

To conclude, the tensile and super-elastic behaviours of the NiTi weldments with and without PWHT were studied in Hanks' solution at 37.5 °C at OCP by tensile and cyclic SSRT. The results were compared with those tested in oil.

The findings in this study indicated that the NiTi weldment showed high susceptibility to hydrogen cracking in Hanks' solution at OCP subjected to mechanical loading, as evidenced by the decrease of breakdown strain and increase of accumulated residual strain when comparing to the results tested in oil. The weldment after heat-treatment at 350 °C (or 623 K) showed improved performances in both the tensile and cyclic SSRT in Hanks' solution with higher breakdown strain and smaller accumulated residual strain recorded. Also, the micro-cracks present in the fracture surface was found to be significantly reduced.

The higher resistance to the hydrogen attack after post-welded heat-treatment was due to the reduced amount of dislocations acting as hydrogen trapping sites and formation of more protective surface passive film. Both of the effects were originating from the precipitation of fine and coherent Ni_4Ti_3 particles.

Acknowledgement

The work described in this article was supported by the research fund from the School of Mechanical and Aerospace Engineering, Queen's University Belfast, Northern Ireland, UK and the Department of Industrial and Systems Engineering, the Hong Kong Polytechnic University, Hong Kong Special Administrative Region, China.

References

[1] T. Duerig, A. Pelton, and D. Stockel, An overview of nitinol medical applications, Mater. Sci. Eng. A 273-275 (1999) 149-160.

[2] N.B. Morgan, Medical shape memory alloy applications - the market and its products, Mater. Sci. Eng. A 378 (2004) 16-23.

[3] K. Yokoyama, K. Hamada, K. Moriyama, K. Asaoka, Degradation and fracture of Ni-Ti super-elastic wire in an oral cavity, Biomater. 22 (2001) 2257-2262.

[4] K. Yokoyama, K. Kaneko, K. Moriyama, K. Asaoka, J. Sakai, and M. Nagumo, Hydrogen embrittlement of Ni-Ti super-elastic alloy in fluoride solution, J. Biomed. Mate. Res. A 65 (2003) 182-187.

[5] K. Yokoyama, T. Ogawa, K. Takashima, K. Asaoka, and J. Sakai, Hydrogen embrittlement of Ni-Ti super-elasticity alloy aged at room temperature after hydrogen charging, Mater. Sci. Eng. A 466 (2007) 106-113.

[6] K. Yokoyama, M. Tomita, and J. Sakai, Hydrogen embrittlement behaviour induced by dynamic martensitic transformation of Ni-Ti super-elasticity alloy, Acta Mater. 57 (2009) 1875-1885.

[7] K. Asaoka, K. Yokoyama, and M. Nagumo, Hydrogen embrittlement of nickel-titanium alloy in biological environment, Metall. Mater. Tran. A. 33 (2002) 495-501.

[8] P. Schlossmacher, T. Haas, and A. Shussler, Laser-welding of a Ni-rich TiNi shape memory alloy: mechanical behavior, J. Phys. IV Coll., C5 (1997) 251-256.

[9] Tuissi, S. Besseghini, T. Ranucci, F. Squatrito, and M. Pozzi, Effect of Nd-YAG laser welding on the functional properties of the Ni-49.6 at.% Ti., Mater. Sci. Eng. A, 273-275 (1999) 813-817.

[10] Y. Ogata, M. Takatugu, T. Kunimasa, K. Uenishi, and K.F. Kobayashi, Tensile strength and pseudo-elasticity of YAG laser spot melted Ti-Ni shape memory alloy wires, Mater. Trans., 45 (2004) 1070-76.

[11] Falvo, F.M. Furgiuele, and C. Maletta, Functional behavior of a NiTi welded joint: two-way shape memory effect, Mater. Sci. Eng. A, 412 (2005) 235-240.

[12] H. Gugel, A. Schuermann, and W. Theisen, Laser welding of NiTi wires, Mater. Sci. Eng. A, 481-482 (2008) 668-671.

[13] M.I. Khan, S.K. Panda, and Y. Zhou, Effects of welding parameters on the mechanical performance of laser welded Nitinol, Mater. Trans., 49 (2008) 2702-2708.

[14] M.I. Khan and Y. Zhou, Effects of local phase conversion on the tensile loading of pulsed Nd:YAG laser processed Nitinol, Mater. Sci. Eng. A, 527 (2010) 6235-6238.

[15] B. Tam, M.I. Khan, and Y. Zhou, Mechanical and functional properties of laser-welded Ti-55.8wt% Ni Nitinol wires, Metall. Mater. Trans. A, 42A (2011) 2166-2175.

[16] Y.T. Hsu, Y.R. Wang, S.K. Wu, and C. Chen, Effect of CO_2 laser welding on the shape-memory and corrosion characteristics of TiNi alloys, Metall. Mater. Trans. A, 32A (2001) 569-576.

[17] X.J. Yan and D.Z. Yang, Corrosion resistance of a laser spot-welded joint of NiTi wire in simulated human body fluids, J Biomed Mater Res A, 77 (2006) 97-102.

[18] X.J. Yan, D.Z. Yang, X.P. Liu, Corrosion behavior of a laser-welded NiTi shape memory alloy, Mater. Charact. 58 (2007) 623-628.

[19] C.W. Chan, H.C. Man, T.M. Yue, Susceptibility to environmentally-induced cracking of laser-welded NiTi wires in Hanks' solution at open-circuit potential, Mater. Sci. Eng. A 544 (2012) 38-47.

[20] C.W. Chan, H.C. Man, T.M. Yue, Effect of annealing on the tensile deformation characteristics of laser-welded NiTi thin foil, Metals and Materials International, 18 (2012) 691-697.

[21] C.W. Chan, H.C. Man, T.M. Yue, Effect of post-weld heat-treatment on the microstructure and cyclic deformation behaviors of the laser-welded NiTi wires, Metall. Mater. Trans. A, 43 (2012) 1956-1965.

[22] C.W. Chan, H.C. Man, T.M. Yue, Parameter optimization on laser welding of NiTi wires by Taguchi method, Laser. Eng. Accepted at 2/6/2012.

[23] C.W. Chan, H.C. Man, T.M. Yue, Effect of post-weld heat-treatment on the oxide film and corrosion behaviors of the laser-welded NiTi wires, Corros. Sci. 56 (2012) 158-167.

[24] ASTM Standard G61-86. Conducting cyclic potentiodynamic polarization measurements for localized corrosion susceptibility in iron-, nickel or cobalt- based alloys. ASTM Standards, Philadephia, PA, USA; 1993.

[25] C.W. Chan, H.C. Man, Laser welding of thin foil nickel–titanium shape memory alloy, Opt. Las. Eng. 49 (2011) 121-126.

[26] C.W. Chan, H.C. Man, T.M. Yue, Effects of process parameters upon the shape memory and pseudo-elastic behaviours of laser-welded NiTi thin foil, Metall. Mater. Trans. A 42 (2011) 2264-2270.

[27] K. Otsuka and C.M. Wayman: Shape Memory Material, Cambridge University Press, Cambridge, United Kingdom, 1998, pp. 49 – 96.

[28] J. Khalil-Allafi, A. Dlouhy, and G. Eggeler, Ni_4Ti_3-precipitalion during aging of NiTi shape memory alloys and its influence on martensitic phase transformations, Acta Mater., 50 (2002) 4255-4274.

[29] T.J. Carter and L.A. Cornish, Hydrogen in metals, Eng. Fail. Anal. 8 (2001) 113-121.

[30] K.Y. Chiu, F.T. Cheng, H.C. Man, Hydrogen effect on the cavitation erosion resistance of AISI 316L stainless steel laser surface-modified with NiTi, Mater. Lett. 61 (2007) 239-243.

[31] A.R. Pelton, J. DiCello, S. Miyazaki, Optimisation of processing and properties of medical grade, Min. Invas. Ther. Allied Technol., 9 (2000) 107-118.

[32] W.H. Zou, X.D. Han, R. Wang, Z. Zhang, W.Z. Zhang, J.K.L. Lai, TEM and HREM study of the interphase interface structure of Ti3Ni4 precipitates and parent phase in an aged TiNi shape memory alloy, Mater. Sci. Eng. A 219 (1996) 142-147.

[33] K. Gall, H. Sehitoglu, Y. Chumlyakov, I. Kireeva, Tension compression asymmetry of the stress-strain response in aged single crystal and polycrystalline NiTi, Acta Mater. 47 (1999) 1203-1217.

[34] K. Gall, H. Sehitoglu, Y. Chumlyakov, I. Kireeva, H.J. Maier, The influence of aging on critical transformation stress levels and martensite start temperatures in NiTi: Part I - aged microstructure and micro-mechanical modeling. J. Eng. Mater. Tech. 121 (1999) 19-27.

[35] K. Gall, H. Sehitoglu, Y. Chumlyakov, I. Kireeva, H.J. Maier, The influence of aging on critical transformation stress levels and martensite start temperatures in NiTi: Part II - discussion of experimental results. J. Eng. Mater. Tech. 121 (1999) 28-37.

[36] K. Otsuka, X. Ren, Physical metallurgy of Ti-Ni-based shape memory alloys, Prog. Mater. Sci. 50 (2005) 511-678.

[37] D. Treppmann, E. Hornbogen, D. Wurzel, The effect of combined recrystallization and precipitation processes on the functional and structural properties of NiTi alloys, J. De. Phys. 5 (1995) 569-574.

[38] H.C. Man, Z.D. Cui, T.M. Yue, Corrosion properties of laser surface melted NiTi shape memory alloy, Scr. Mater. 45 (2001) 1447-1453.

Tables and Figures

Table 1. DSC phase transformation temperatures of various samples

Samples	Transformation Temperatures (°C)			
	Heating Curve		Cooling Curve	
	A_s	A_f	M_s	M_f
Base Metal (As-received)	−3.6	8.8	2.2	−7.0
Weld Zone (As-welded)	−20.6	−5.8	−40.5	−52.3
Weld Zone (Heat-treated)	20.3	29.4	8.5	−3.2
The transformation temperatures are denoted as A_s (Austenite start), A_f (Austenite finish), M_s (Martensite start), and M_f (Martensite finish)				

Table 2. Corrosion parameters of various samples in Hanks' solution at 37.5 °C

Corrosion Parameters	As-received	As-welded	Heat-treated
Ecorr (mVSCE)	−243	−310	−268
Epit (mVSCE)	403	264	391
Icorr (nA)	200	560	260

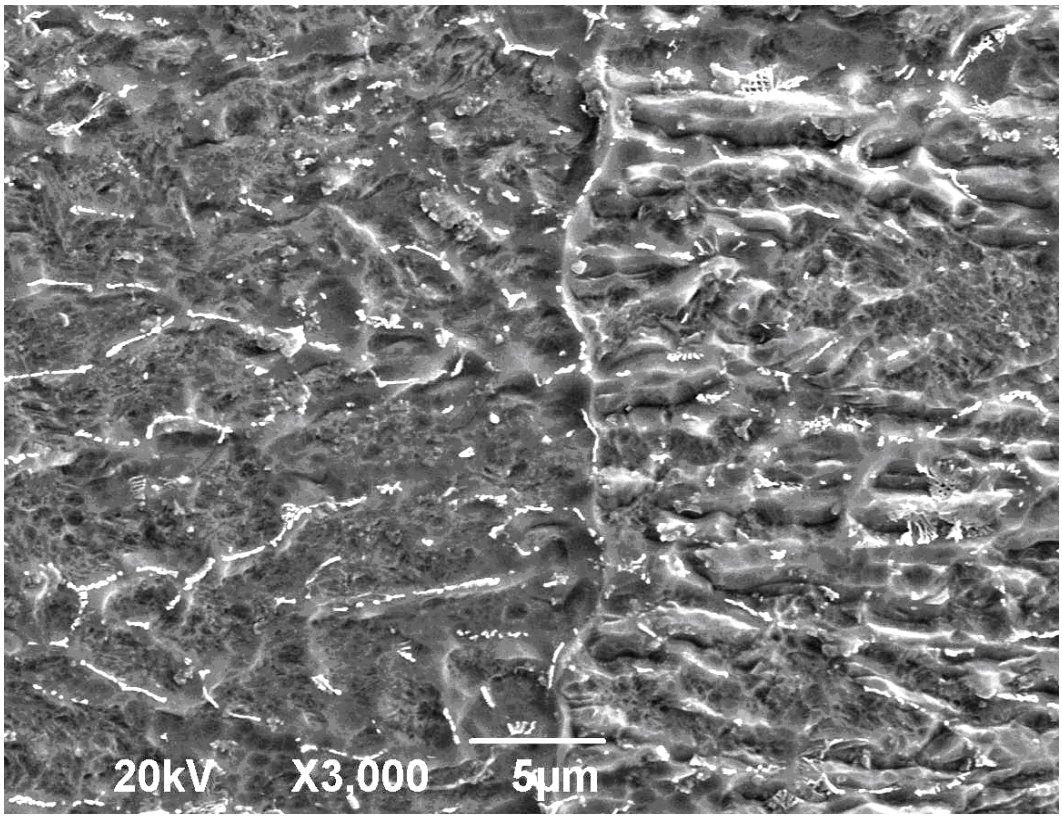

(a) Weld Zone (WZ)

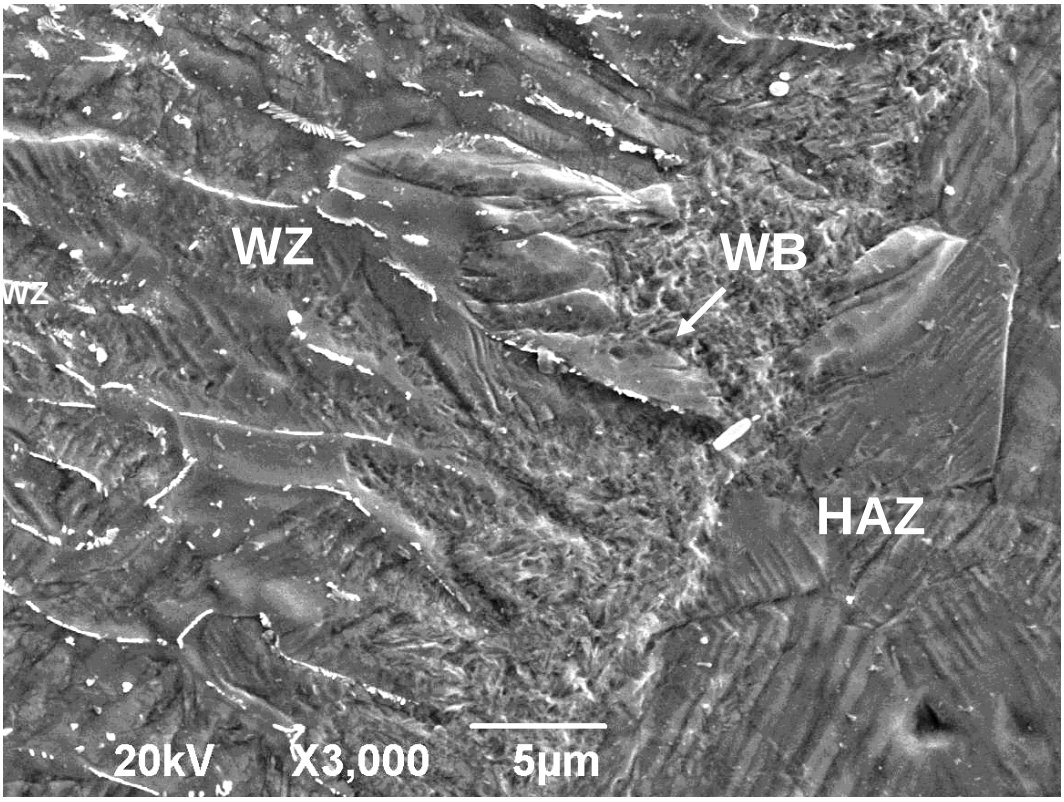

(b) Weld Boundary (WB) between WZ and HAZ

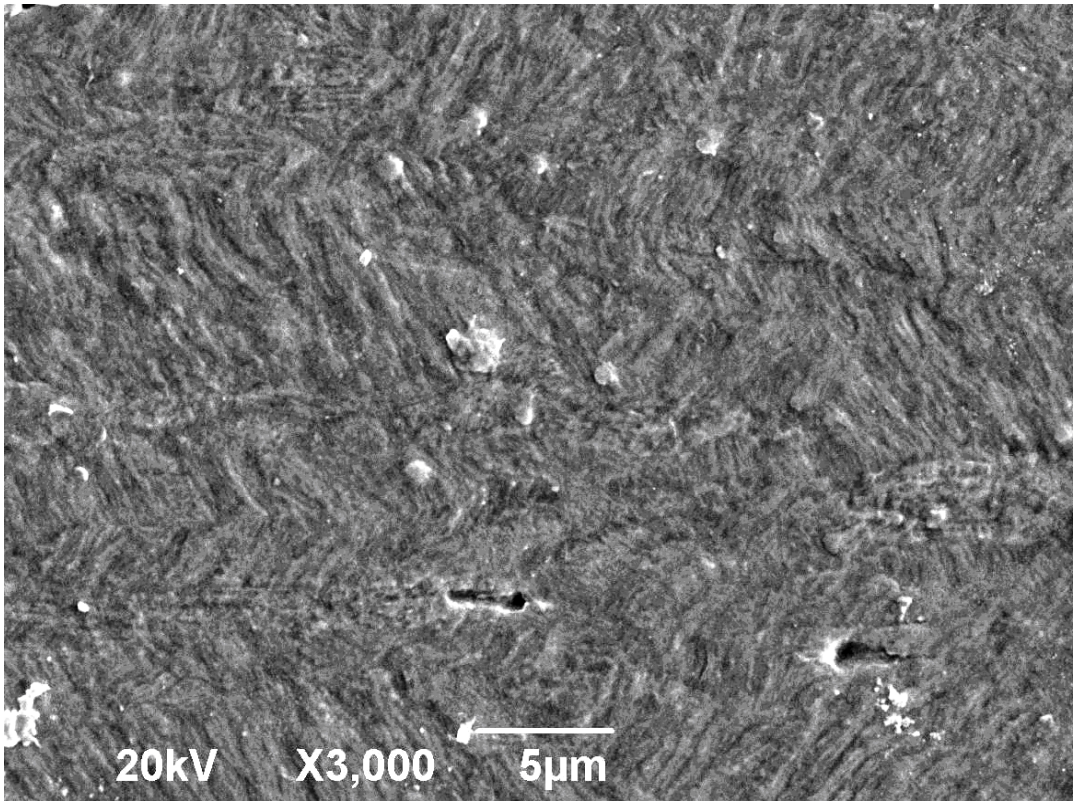

(c) Base metal (BM)

Fig. 1. SEM micrographs for the (a) WZ, (b) weld boundary WZ and HAZ, and (c) BM in the heat-treated sample

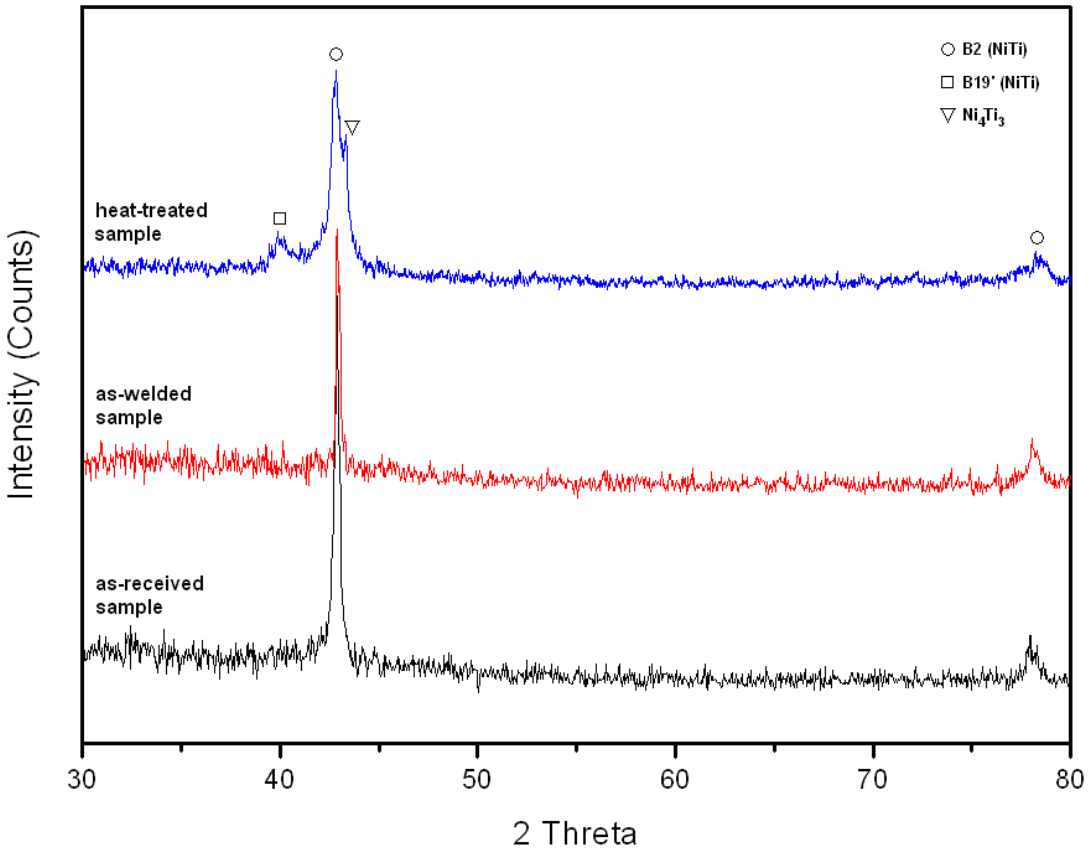

Fig. 2. XRD patterns for different samples

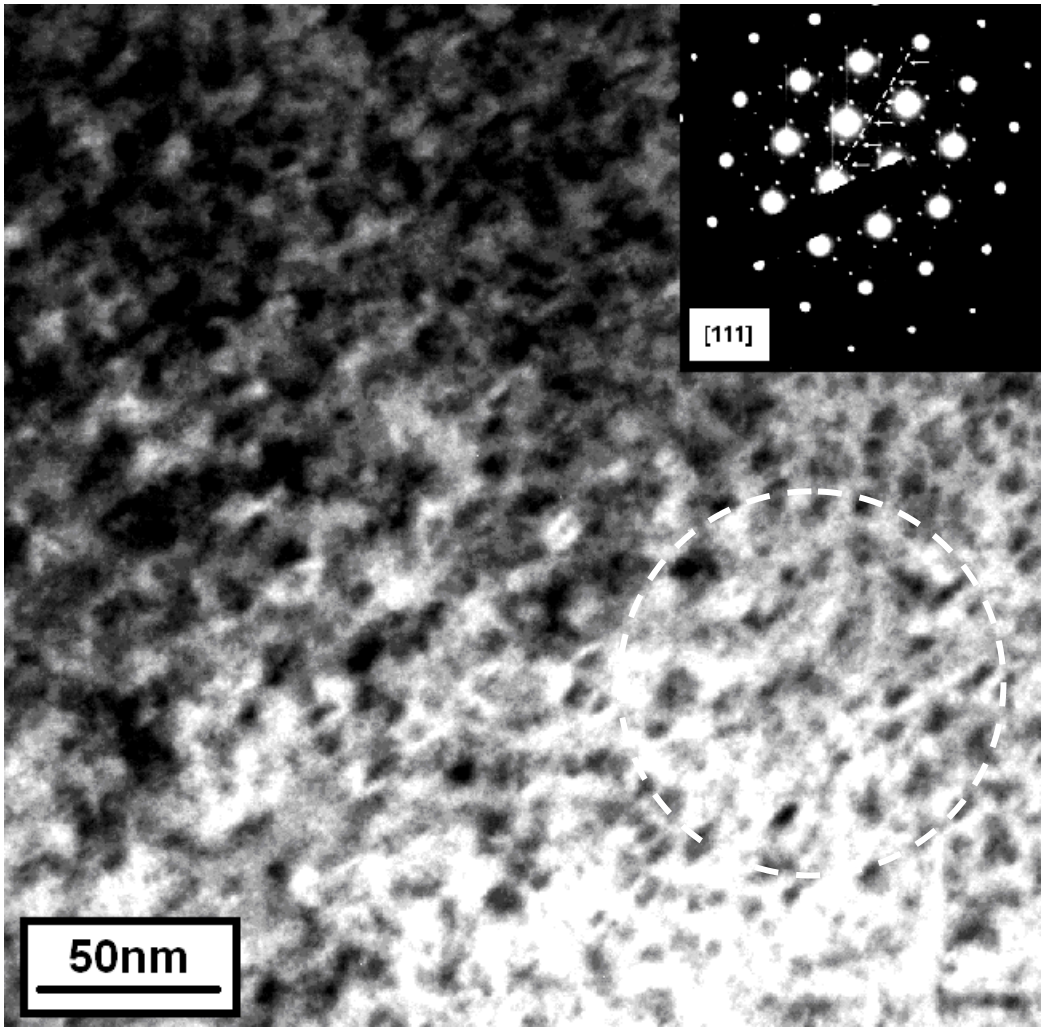

Fig 3. TEM micrograph for the WZ in the heat-treated sample and the corresponding SADP of Ni_4Ti_3 precipitates

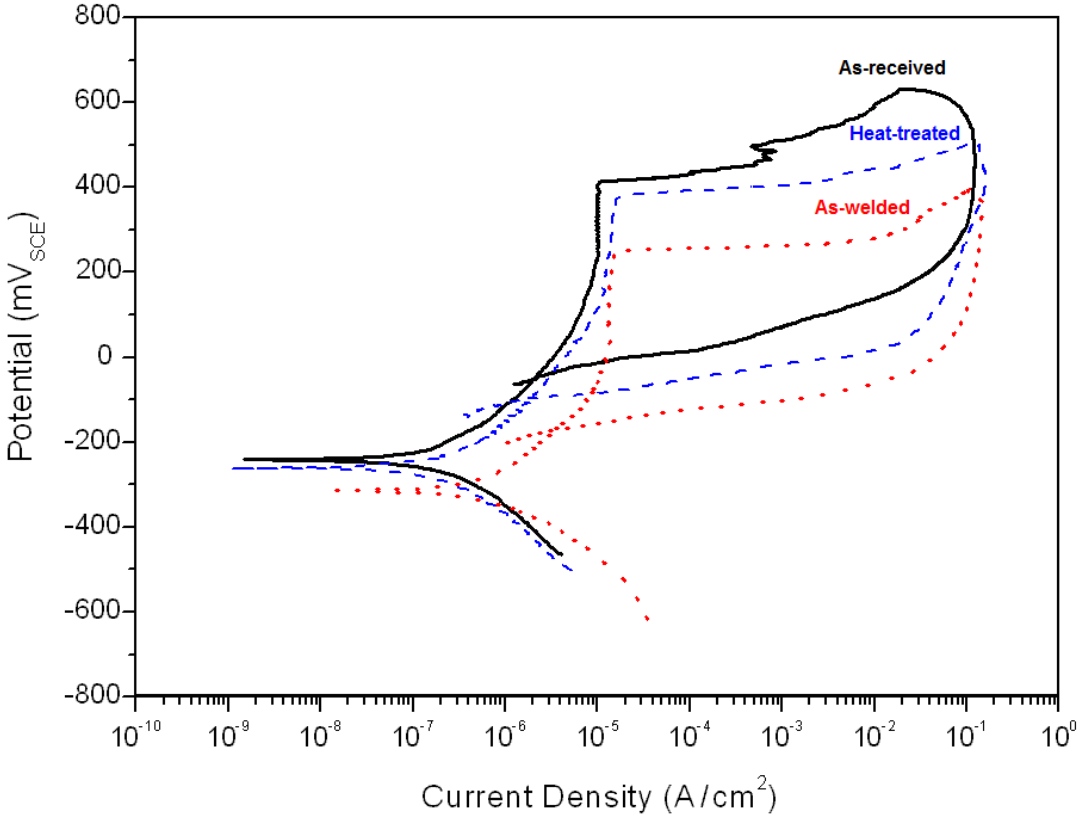

Fig. 4. Cyclic polarization curves for samples in Hanks solution at 37.5 °C

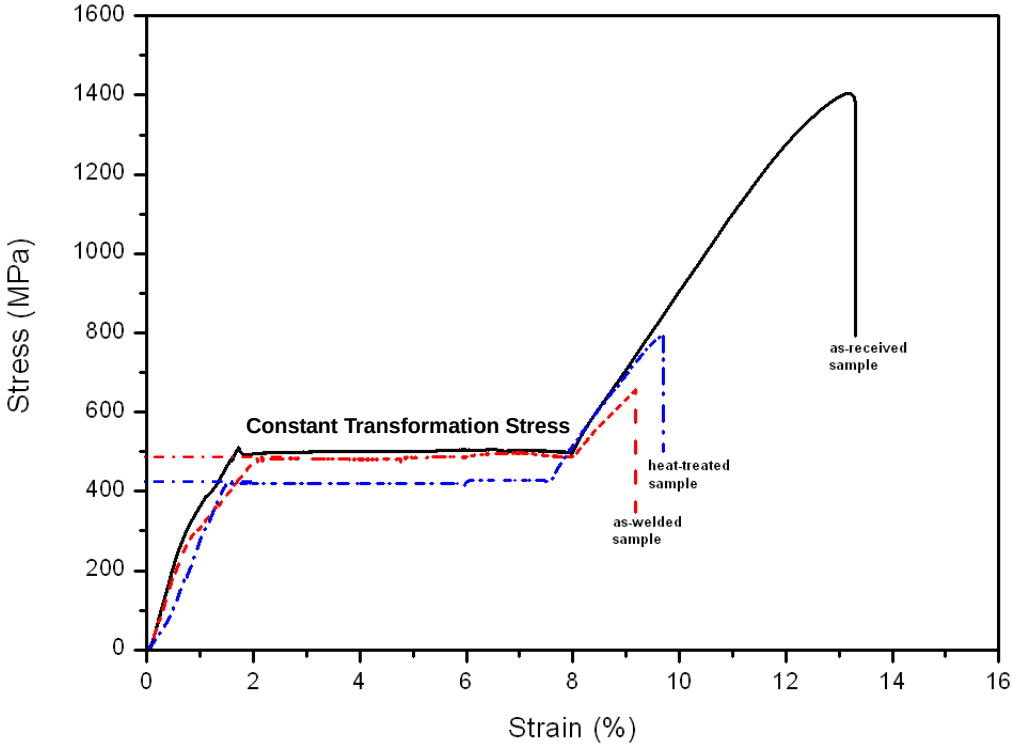

Fig. 5. Stress-strain curves for various samples in oil at 37.5 °C

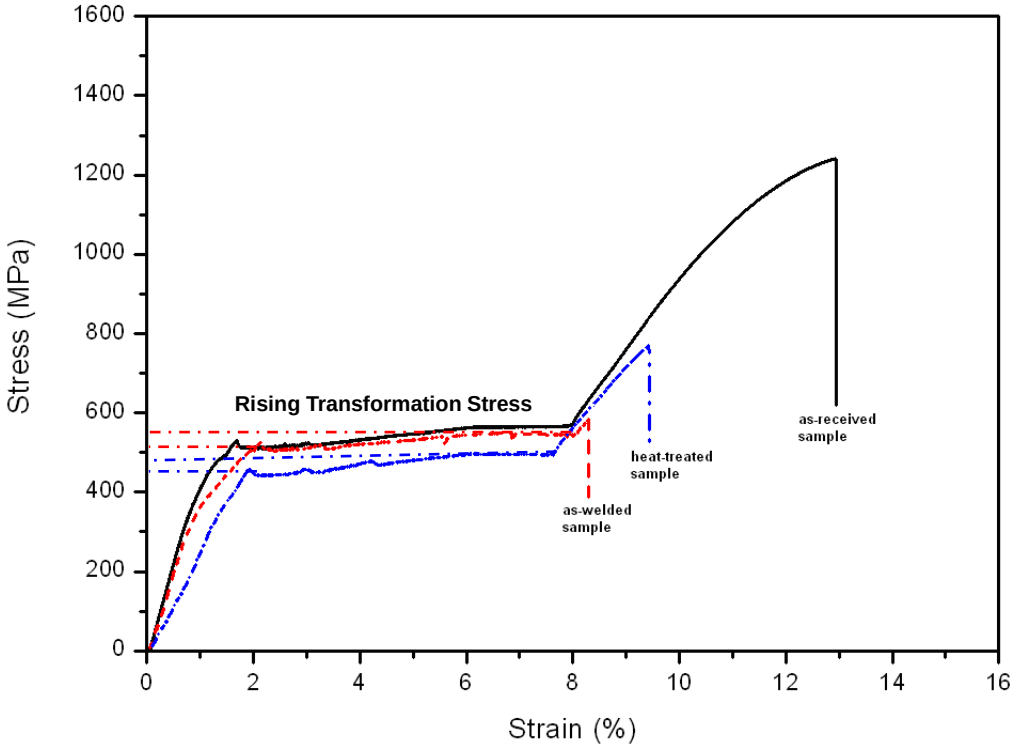

Fig. 6. Stress-strain curves for various samples in Hanks' solution at OCP at 37.5 °C

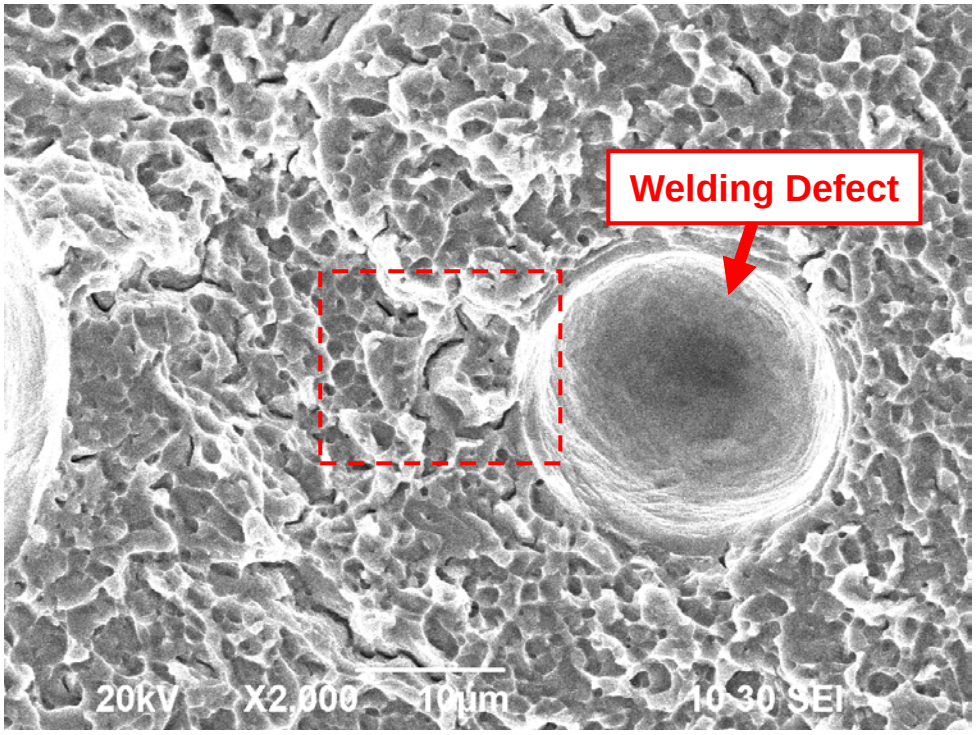

(a) Micro-cracks and welding defect in the fracture surface of the as-welded sample

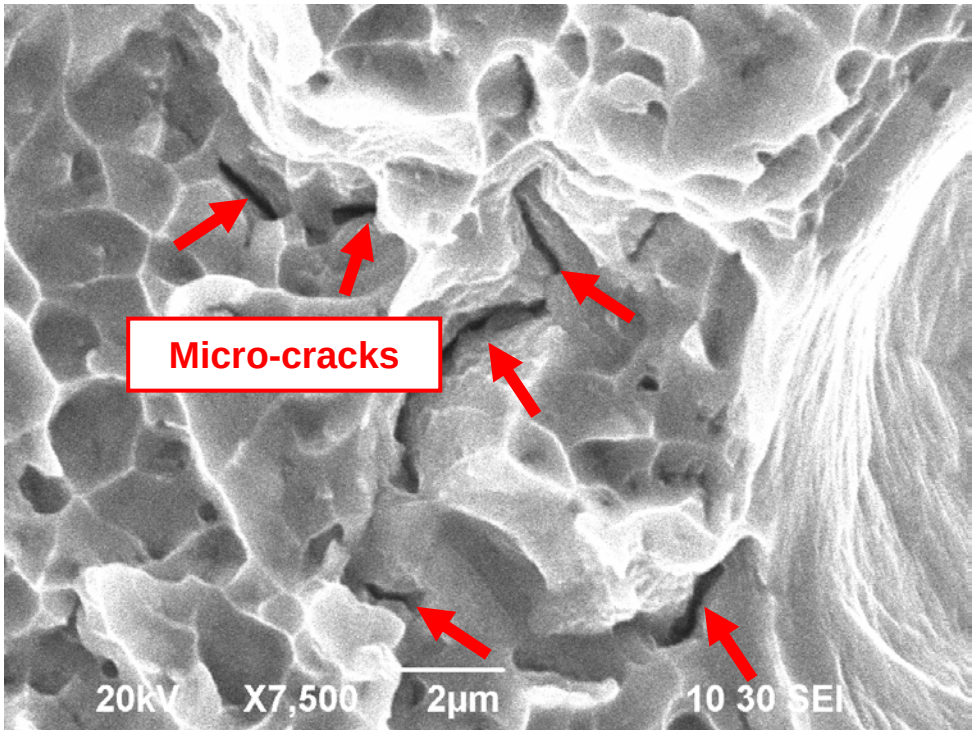

(b) Higher magnification of the micro-cracks in the red box of 7 (a)

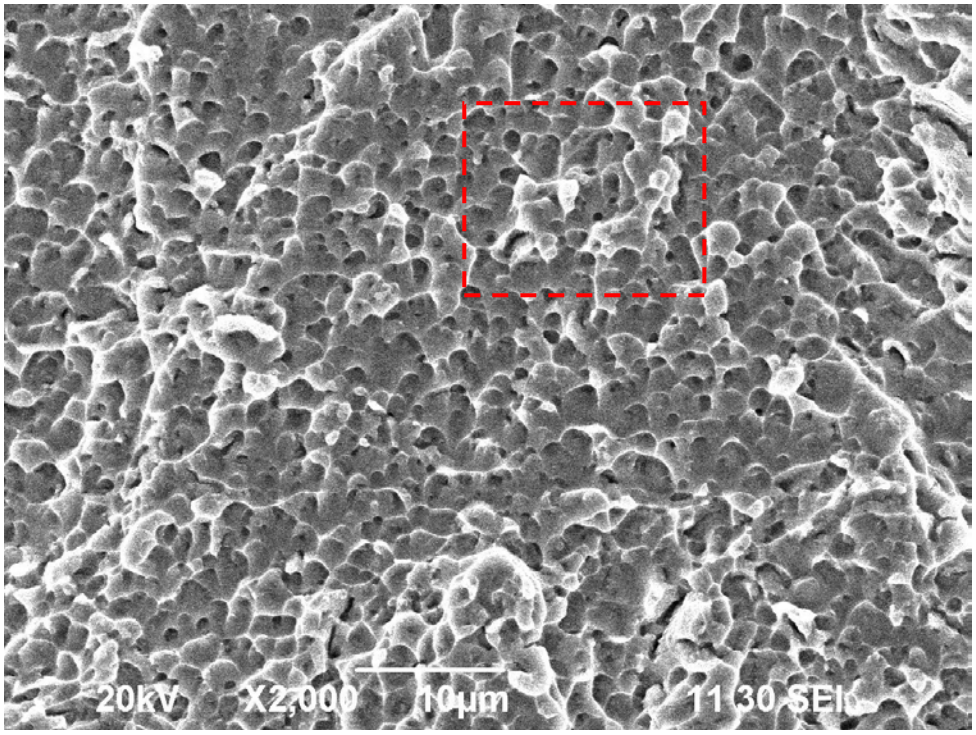

(c) Micro-cracks and welding defect in the fracture surface of the as-welded sample

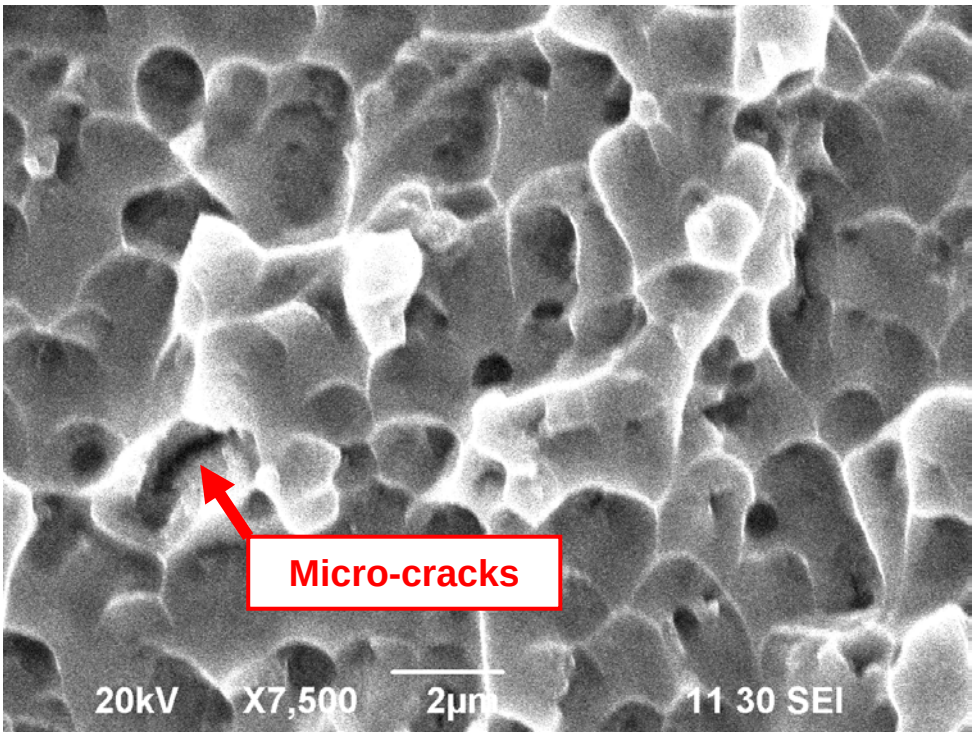

(d) Higher magnification of the micro-cracks in the red box of 7 (c)

Fig 7. SEM fractographs for the (a-b) as-welded and (c-d) heat-treated samples after cyclic SSRT in Hanks' solution

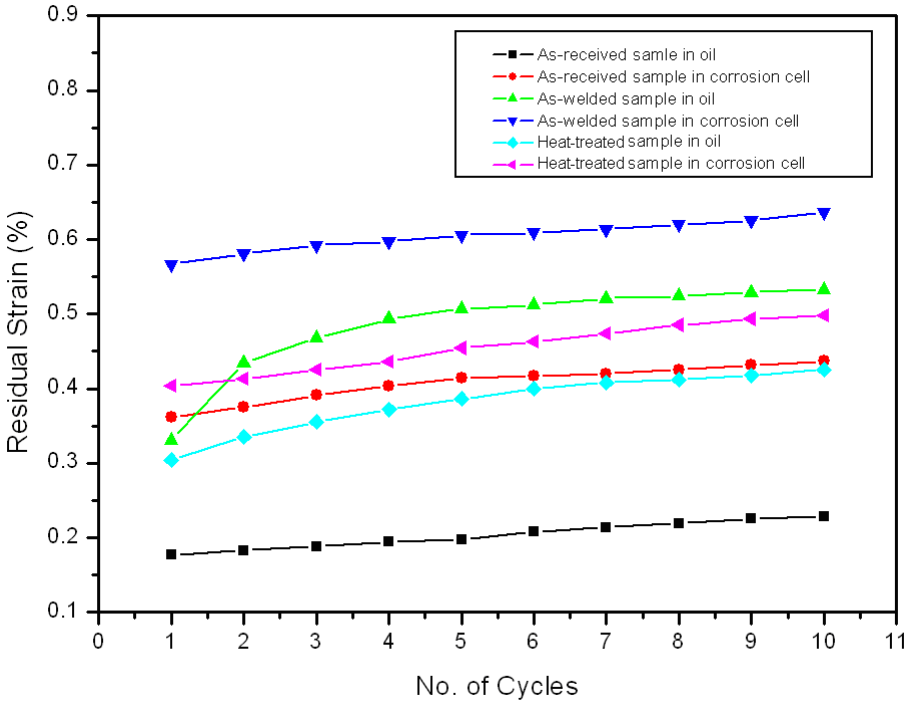

Fig. 8. Accumulated residual strain curves for various samples after cyclic SSRT in oil and Hanks' solution at OCP at 37.5 °C

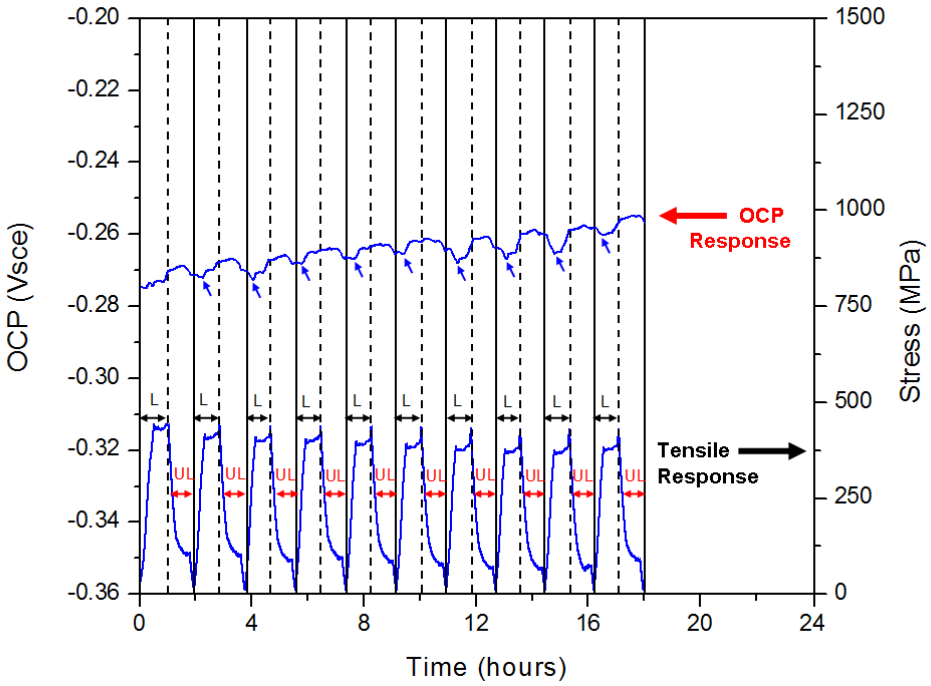

Fig. 9. In-situ OCP curves for various samples during cyclic SSRT in Hanks' solution

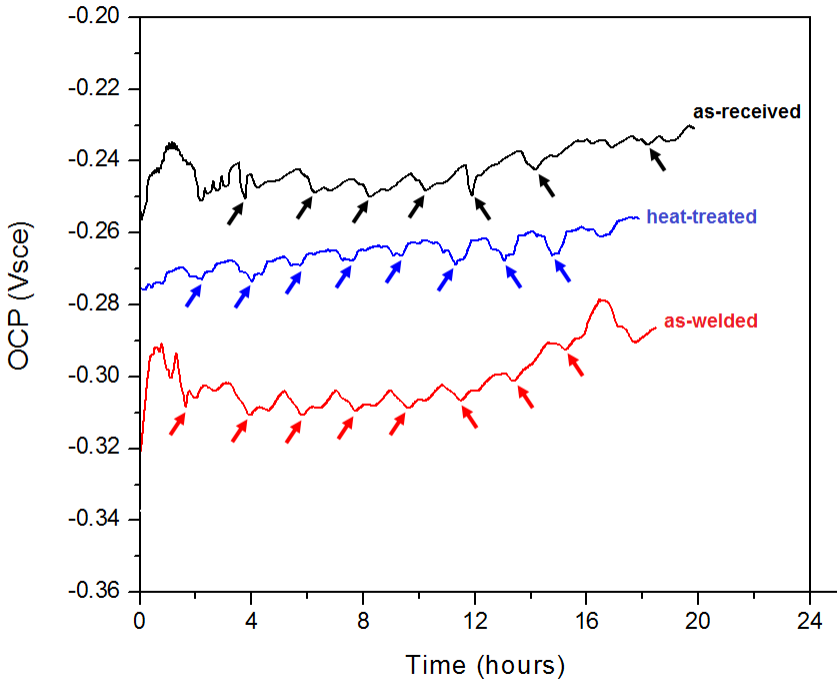

Fig. 10. In-situ OCP and stress-strain curves for the heat-treated sample during cyclic SSRT in Hanks' solution

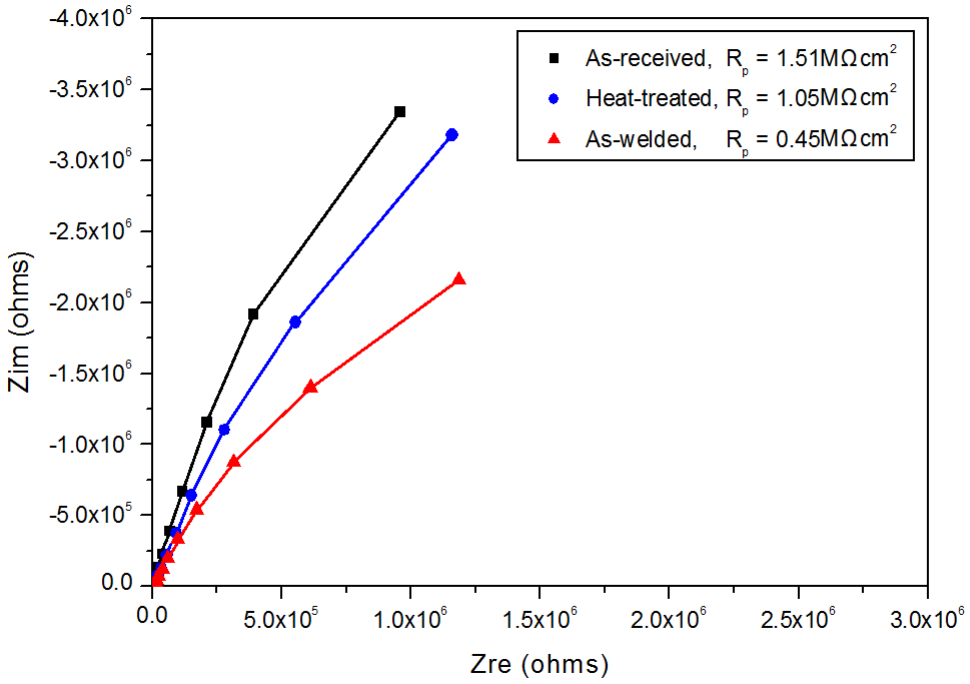

(a) Nyquist plots after cyclic SSRT

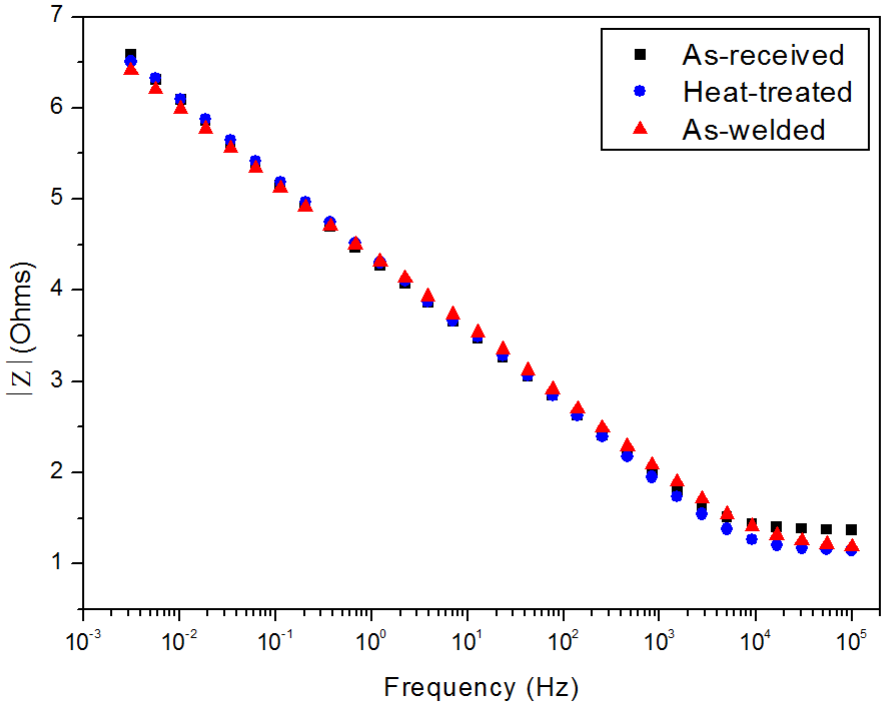

(b) Bode plots after cyclic SSRT

Fig. 11. (a) Nyquist plots and (b) Bode plots of EIS measurements for various samples in Hanks' solution at OCP after cyclic SSRT